Journal of ELECTRONIC MATERIALS, Vol. 42, No. 11, 2013
DOI: 10.1007/s11664-013-2798-2
© 2013 TMS

High-Performance M/LWIR Dual-Band HgCdTe/Si Focal-Plane Arrays

M.F. VILELA,[1,2] K.R. OLSSON,[1] E.M. NORTON,[1] J.M. PETERSON,[1] K. RYBNICEK,[1] D.R. RHIGER,[1] C.W. FULK,[1] J.W. BANGS,[1] D.D. LOFGREEN,[1] and S.M. JOHNSON[1]

1.—Raytheon Vision Systems, 75 Coromar Drive, Goleta, CA 93117, USA. 2.—e-mail: mauro_f_vilela@raytheon.com

Mercury cadmium telluride (HgCdTe) grown on large-area silicon (Si) substrates allows for larger array formats and potentially reduced focal-plane array (FPA) cost compared with smaller, more expensive cadmium zinc telluride (CdZnTe) substrates. In this work, the use of HgCdTe/Si for mid-wavelength/long-wavelength infrared (M/LWIR) dual-band FPAs is evaluated for tactical applications. A number of M/LWIR dual-band HgCdTe triple-layer *n-P-n* heterojunction device structures were grown by molecular-beam epitaxy (MBE) on 100-mm (211)Si substrates. Wafers exhibited low macrodefect densities (<300 cm^{-2}). Die from these wafers were mated to dual-band readout integrated circuits to produce FPAs. The measured 81-K cutoff wavelengths were 5.1 μm for band 1 (MWIR) and 9.6 μm for band 2 (LWIR). The FPAs exhibited high pixel operability in each band with noise-equivalent differential temperature operability of 99.98% for the MWIR band and 98.7% for the LWIR band at 81 K. The results from this series are compared with M/LWIR FPAs from 2009 to address possible methods for improvement. Results obtained in this work suggest that MBE growth defects and dislocations present in devices are not the limiting factor for detector operability, with regards to infrared detection for tactical applications.

Key words: HgCdTe, dual band, FPAs, Si substrates, infrared detectors, molecular-beam epitaxy (MBE)

INTRODUCTION

HgCdTe is the material of choice for developing high-performance infrared (IR) detectors. IR detection can be divided into two applications: tactical and strategic. Tactical applications typically observe warm targets with high background irradiance. On the other hand, strategic (or space) applications typically deal with cool targets with low background irradiance. Raytheon Vision Systems (RVS) has been developing HgCdTe devices for IR detection from short-wave infrared (SWIR) to long-wave infrared (LWIR) on both lattice-matched and lattice-mismatched substrates for more than three decades.[1–6] Single- and dual-color focal-plane arrays (FPAs) have been developed with excellent quantum efficiency and operability.[7] RVS is capable of producing devices on large-area substrates with three production systems: a RIBER Epineat capable of a maximum 125-mm-diameter wafer and two VG-V100 devices capable of a maximum 200-mm-diameter wafer. HgCdTe epitaxially grown on large-area Si substrates allows IR FPAs to be scaled to larger formats than are possible with the largest (80 mm × 80 mm) CdZnTe substrates presently available. Large Si substrates also allow higher array count per wafer for reduced die cost.

To our knowledge, only one other group has reported results regarding dual-band M/LWIR HgCdTe grown on alternative substrates to CdZnTe. Selex has reported results for M/LWIR FPAs based on

(Received March 29, 2013; accepted September 12, 2013; published online October 8, 2013)

HgCdTe grown on 75-mm GaAs substrates by metalorganic vapor-phase epitaxy (MOVPE).[8,9]

This paper reports advancements at RVS in dual-band FPA technology using HgCdTe grown on Si substrates. This growth technology has substantial promise for reducing FPA cost for tactical applications, but significant improvement is still necessary for viability of this technology for strategic applications. For strategic applications, the higher dislocation density presented for HgCdTe material grown on lattice-mismatched substrate needs to be decreased by orders of magnitude. Therefore, all discussions and results in this paper are only valid for tactical applications.

A series of M/LWIR dual-band HgCdTe *n-P-n* triple-layer heterojunction (TLHJ) device structures were grown on 100-mm (211)Si substrates with a ZnTe/CdTe buffer layer. The target 78-K cutoff wavelengths were 5.3 μm and 9.5 μm for the MWIR and LWIR band, respectively. The fabrication process for these dual-band HgCdTe-on-Si detectors utilizes mature fabrication processes at RVS. Selected detector and readout integrated circuit (ROIC) arrays were hybridized to fabricate FPAs. The better FPAs of those tested demonstrated noise-equivalent differential temperature (NEDT) operabilities up to 99.98% for the MWIR band and 98.7% for the LWIR band at 81 K, under *f*/3 background. It is important to note that this result was reproduced in more than one wafer for this series. Also, it is important to mention that the devices obtained in this work need to be tested for long run operation with proven stability over temperature cooldown cycles, from 300 K to 78 K. Such stability study lies beyond the scope of this work, which solely presents results for material quality and consequent performance. The stability of these devices over temperature cooldown cycles is under investigation and will be the subject of a future publication.

DUAL-BAND DETECTOR DESCRIPTION

The current Raytheon dual-band detector is based on a bias-selectable back-to-back diode structure.[10] The single-mesa architecture for the dual-band detector with its single contact per unit cell is shown in Fig. 1a. This detector utilizes an MBE-grown *n-P-n* TLHJ structure. Operated with backside illumination, the bottom *n*-type layer absorbs the shorter-wavelength (band 1) radiation. Longer-wavelength (band 2) radiation passes through the bottom *n*-type absorber and middle p^+ layer and is detected by the top photodiode, as shown schematically in Fig. 1b.

The dual-band mesas are formed using inductively coupled plasma (ICP). An example image of a representative dual-band detector is shown in Fig. 2a. The dry etch process produces a smooth and steep sidewall, as shown in Fig. 2b. This structure achieves approximately 100% optical fill factor in each band due to total internal reflection of incident radiation off the mesa sidewalls. The nature of the RVS detector design and operation makes each band 2 pixel fully isolated and band 1 pixels partially isolated, which minimizes spatial crosstalk between pixels. The polarity of the bias across the structure determines which junction is photoactive and thereby the spectral band of the detector (see schematic in Fig. 1a). The bias switching is performed by the dual-band ROIC. The bias value used for each band evaluation is +150 mV for the LWIR and −50 mV for the MWIR.

MATERIAL GROWTH AND CHARACTERIZATION

The M/LWIR dual-band *n-P-n* TLHJ HgCdTe structures were grown on 100-mm (211)Si wafers in a Riber Epineat MBE system using CdTe, ZnTe, and Te solid sources and a liquid Hg source. Elemental sources of indium and arsenic were used for *n*-type and *p*-type doping, respectively. The 100-mm (211)Si substrates were prepared for growth using a hydrofluoric-acid-based process. A thin ZnTe nucleation layer followed by a CdTe buffer layer were used as a template for the HgCdTe device layers; details of the ZnTe/CdTe buffer layer can be found in Refs. 6 and 11. Once the Si substrate had been introduced, all layers were grown without wafer removal from the MBE system. The RVS heteroepitaxial HgCdTe/Si technology has been well documented in earlier publications.[5,6,11]

The layers were characterized using room-temperature Fourier-transform infrared (FTIR) transmission mapping measurements coupled with modeling of the transmission spectra[12] to extract layer thickness and the MWIR (band 1) and LWIR (band 2) cutoff wavelengths projected for temperature of 78 K. The macrodefect density was measured using an August Technology NSX105 automated defect inspection system which enables full wafer mapping.[13] A representative piece of each growth wafer in the series was selected for destructive analysis by layer dislocation density inspection. The dislocation density was determined by subjecting the surface of the samples to a decorative etch, as proposed by Benson et al.,[14] to develop the dislocations present at the surface. Using a successive controlled dip wet etch in a diluted bromine-methanol solution followed by the decorative etch, it is possible to track the variation of dislocation density through the entire epitaxially grown device as a function of depth.

By looking at the parallels between results obtained with wafers which were processed into 640 × 480 detector arrays and smaller test structure arrays in 2009 and in this 2012 work, trends could be found to indicate the direction for further improvements in device performance. A special effort was made to use the same grown structure (design and epitaxial phase) and the same sequence

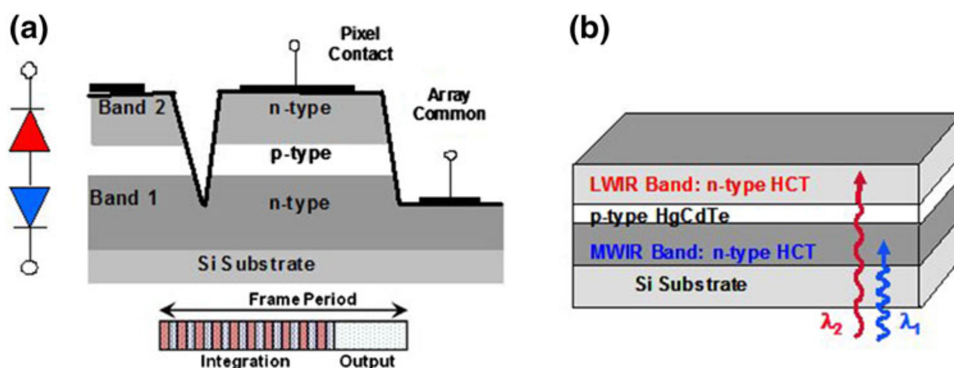

Fig. 1. (a) Single-mesa architecture for the dual-band detector with a single contact per unit cell, also showing a schematic of the back-to-back diode structure. The polarity of the bias across the structure determines which junction is photoactive; a schematic of the bias switching is shown at the bottom, with blue color representing band 1 and red color representing band 2; (b) backside-illumination design with the bottom *n*-type layer absorbing the shorter-wavelength (band 1) radiation while longer-wavelength (band 2) radiation passes through the bottom *n*-type absorber and middle p^+ layer before being detected by the top photodiode.

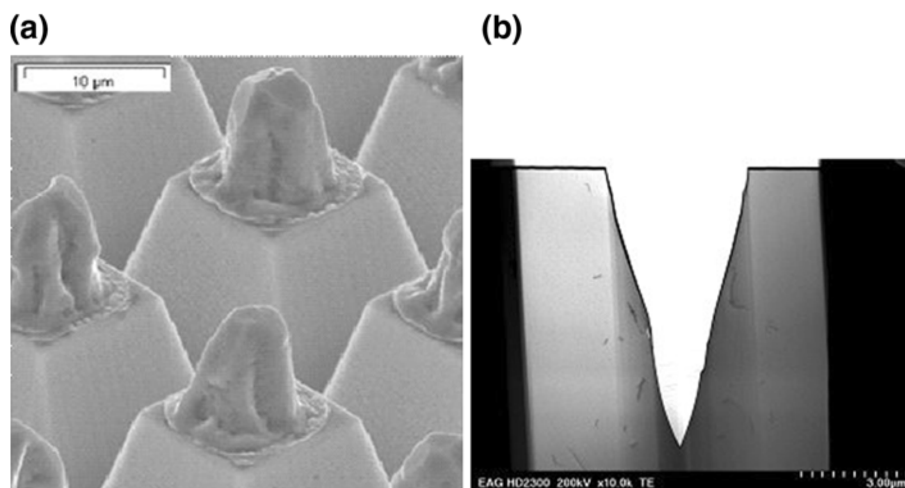

Fig. 2. (a) Representative dual-band detector with 20 μm pitch; (b) transmission electron microscopy (TEM) profile showing that the dry etch process produces a smooth and steep sidewall.

of process steps (fabrication phase) in both the 2009 and 2012 studies. The first characterization step, i.e., FTIR, showed that structures obtained in 2009 and 2012 were functionally identical, with cutoff values comparable and inside the experimental error. The target 78-K cutoff wavelengths were 5.3 ± 0.2 μm and 9.5 ± 0.2 μm for the MWIR and LWIR band, respectively. MBE growth defects are a possible limiting factor for detector performance. Therefore, the epitaxial growth defect density is a characteristic that should be compared and analyzed. Figure 3 shows the typical defect density August maps obtained for M/LWIR wafers in 2009 and 2012. As observed in Fig. 3, defect densities are below 300 cm^{-2} for both the 2009 and 2012 studies. Wafers grown in 2009 show a slightly lower defect density ($\sim$100 cm^{-2}) compared with their counterparts from 2012 ($\sim$250 cm^{-2}). We do not expect a significant (or even measurable) operability difference between these two defect density levels for any FPA with pitch smaller than 60 μm, as shown below. If growth defects are a limiting factor for device performance, it is expected that detector performance metrics obtained in the 2009 series should be better than their 2012 counterparts, but as shown in a later section, the opposite result is obtained. The dislocation density presented in the active region of detectors is another physical parameter that should influence detector performance. Several reports regarding detector performance claim that dislocation density is the main factor limiting LWIR and very long-wave infrared (VLWIR) detector performance.[15–18] Due to the very large lattice and thermal mismatch between the Si substrate and HgCdTe material, a much higher dislocation density is present for devices grown on Si substrates compared with HgCdTe material grown on cadmium zinc telluride (CZT) lattice- and thermally matched substrates. The dislocation density for HgCdTe grown on CZT substrates is under 10^5 cm^{-2} (typically 5×10^4 cm^{-2}), while for HgCdTe grown on Si substrates, the dislocation

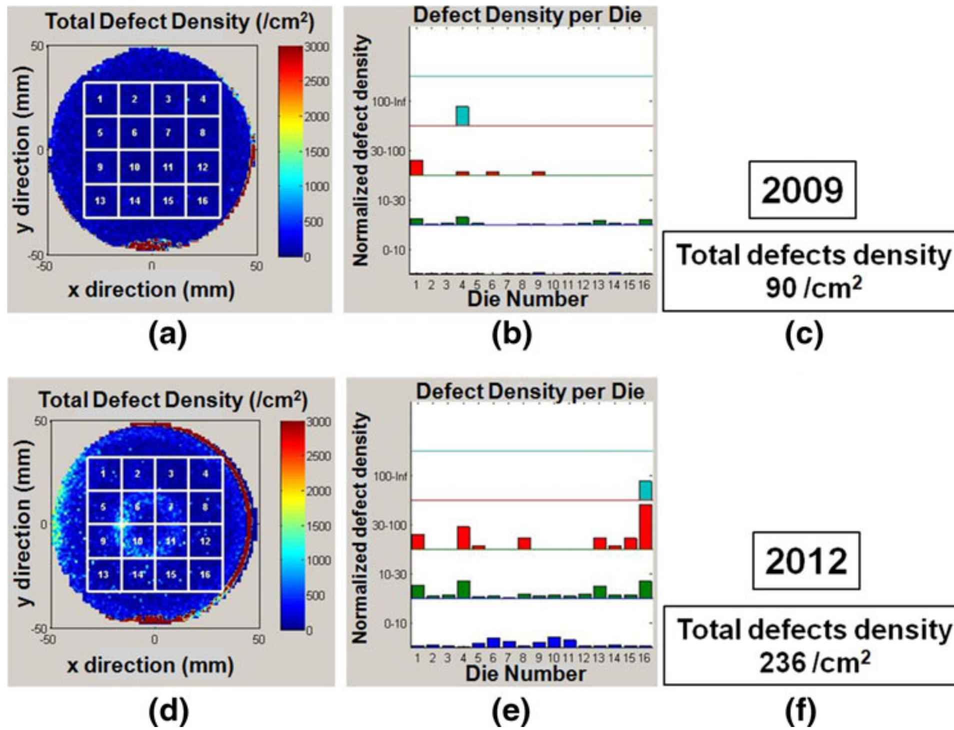

Fig. 3. Defect density maps obtained for M/LWIR wafers in 2009 (a–c) and 2012 (d–f). (a, d) Color diagram showing the density and location of wafer defects with die position superimposed. (b, e) Normalized defect density per die for four different classes of defects (class I: defect diameter from 0 μm to 10 μm; class II: defect diameter from 10 μm to 30 μm; class III: defect diameter from 30 μm to 100 μm; class IV: defect diameter > 100 μm; the count limits are: class I, 2000/cm^2; class II, 200/cm^2; class III, 5/cm^2; class IV, 1/cm^2). (c, f) Overall wafer defect density counts per class and total.

density is typically in the 10^7 cm^{-2} range. The dislocation density can be minimized by growing thick CdTe buffer layers. Figure 4 shows the influence of the CdTe thickness on the dislocation density of HgCdTe grown on top of it. A half-order-of-magnitude improvement is obtained with a thick CdTe buffer layer ($t > 7$ μm) compared with a thin CdTe buffer layer ($t < 2$ μm). Both the 2009 and 2012 series present similar dislocation densities at the surface of $\sim 5 \times 10^6$ cm^{-2}. Other factors (not discussed here) can also influence the dislocation density, such as annealing patterns[19,20] or introducing highly articulated structures.[21]

After the MBE growth, each wafer was characterized by FTIR, had its defect density analyzed via the August mapping tool, and underwent visual inspection by optical microscope; if the wafer passed all initial qualification criteria, it was sent to the processing department for FPA fabrication.

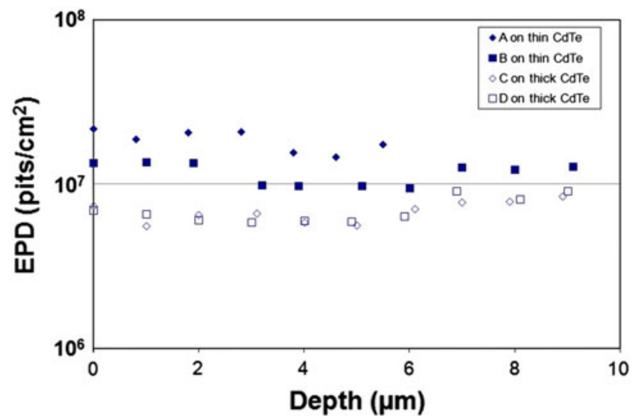

Fig. 4. Variation of dislocation density as a function of depth, showing the influence of CdTe thickness on the dislocation density of HgCdTe grown on top of it. Full symbols are used for thin CdTe buffer layers ($t \leq 2$ μm), and open symbols are used for thick CdTe buffer layers ($t \geq 7$ μm). The origin of the depth axis represents the surface of the wafer.

ARRAY FABRICATION AND TESTING

A number of M/LWIR dual-band HgCdTe/Si layers were processed into detector arrays and small test structure arrays. An example image of a representative dual-band detector is shown in Fig. 2a. Detector fabrication began with mesa delineation of the individual pixels using ICP dry etching followed by patterning, metal deposition, surface passivation, and indium bumps. At the end of wafer processing, the individual detector arrays were diced from each wafer and hybridized to dual-band Si ROIC arrays to form dual-band FPAs. Small detector test arrays (variable-area structures) were hybridized to sapphire fanout boards to form test structure assemblies (TSAs) for direct testing of

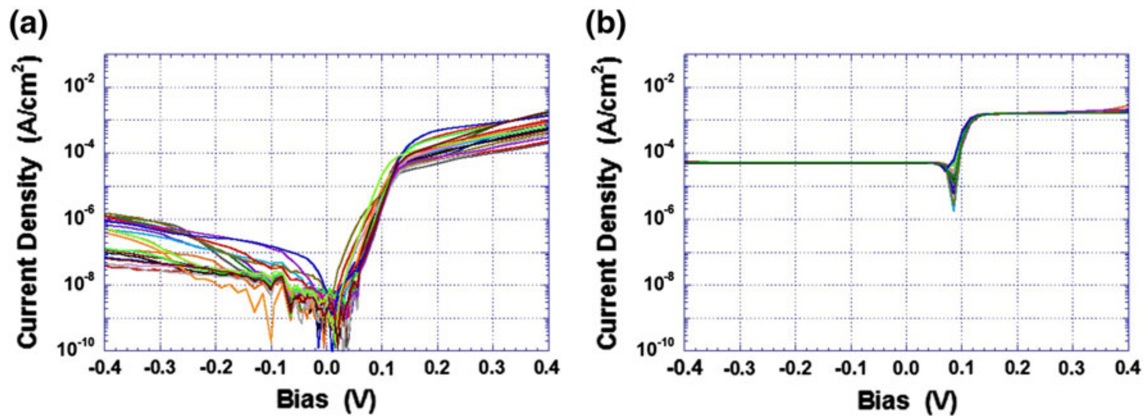

Fig. 5. *I*–*V* curves obtained for 2012 devices, under no radiation flux (a) and under radiation flux (b) at 78 K. Leakage current is very low without flux, but ideal diffusion-limited diode behavior is clearly not shown. The shape of the *I*–*V* curve improves and maintains the low leakage current under flux. It can be observed from these curves that, for all the different dies tested, for the same test structure, a uniform response is obtained, attesting to the uniformity of the RVS detector process.

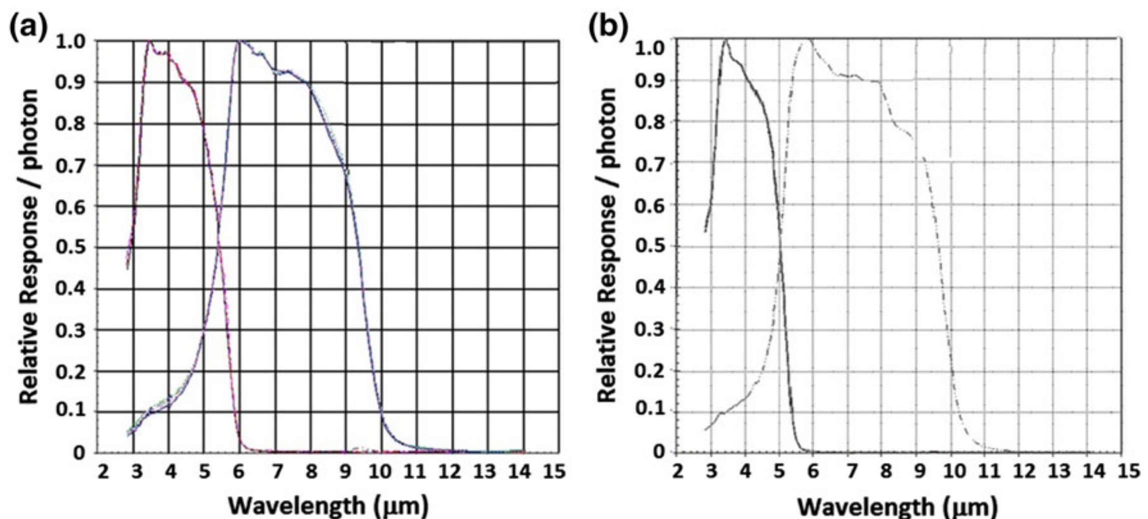

Fig. 6. Spectral response for devices obtained in (a) 2009 at 78 K with MW bias of −50 mV and LW bias of 150 mV and (b) 2012 at 78 K with MW bias of −50 mV and LW bias of 150 mV. Very similar spectral responses are observed for both bands.

detector performance (current–voltage and spectral response) in a cryogenic Dewar.

RESULTS AND DISCUSSION

Figure 5 shows the *I*–*V* curves obtained from the 2012 series of devices, under no radiation flux and under radiation flux at 78 K. Devices from the 2009 series presented very similar *I*–*V* curves with no distinction observed at the same temperature compared with the 2012 devices. Devices from both 2009 and 2012 were similar and had the same motif of 40 μm $\times$ 40 μm. Very low leakage current and very uniform patterns were common characteristics for both sets of devices. However, from Fig. 5a, the *I*–*V* curve under no radiation flux presents a clear deviation from the diffusion-limited behavior of an ideal diode. This deviation from ideality prevents the use of HgCdTe grown on this mismatched substrate for strategic applications.

The spectral responses for 2009 and 2012 devices were highly comparable, as shown in Fig. 6. A minor difference in the cutoff values for both bands is observed.

For tactical applications, the NEDT is widely used as a figure of merit for FPA system performance. The operability of an IR detector array is defined by the number or percentage of defective pixels in the array. Highly uniform arrays have a smaller number of bad pixels, and a pixel is defined as defective if its NEDT characteristic is significantly different from the average. In this work a defective pixel is defined as a pixel having more than twice the median NEDT value. Figure 7 shows a comparison between the MWIR operability of 99.96% (85 K, *f*/3.5 background) of the 2009 series and the 99.98%

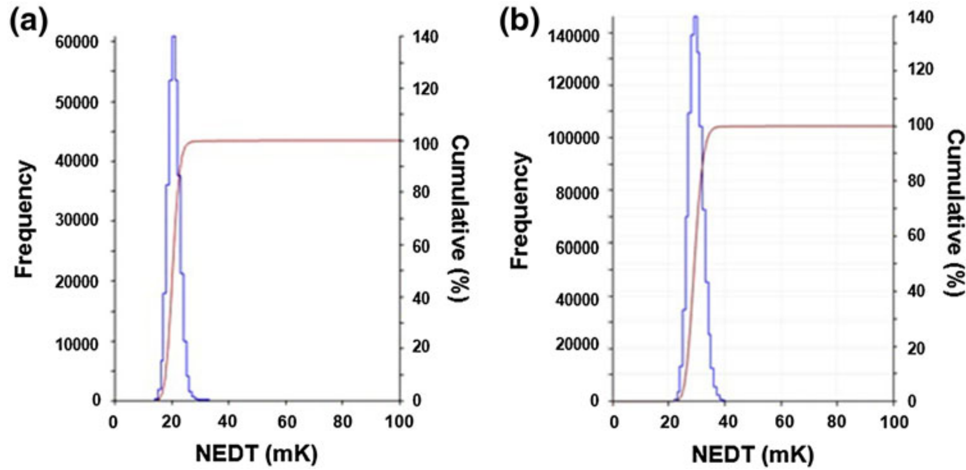

Fig. 7. Operability of (a) 99.96% for the 2009 series MWIR [85 K, *f*/3.5 background, integration time (T_{int}) 4.9 ms, cutoff = 5.5 μm, median NEDT = 20.6 mK] and (b) 99.98% for the 2012 series MWIR [81 K, *f*/3.0 background, integration time (T_{int}) 7.3 ms, cutoff = 5.1 μm, median NEDT = 29.6 mK]. No significant difference between the excellent 2009 and 2012 MWIR performance is observed.

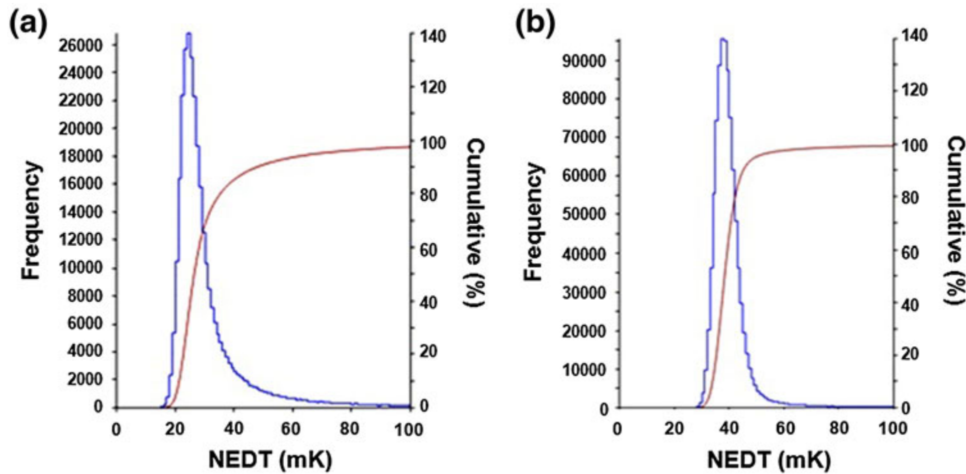

Fig. 8. Operability of (a) 96.1% for the 2009 series LWIR [85 K, *f*/3.5 background, integration time (T_{int}) 469 μs, cutoff = 9.4 μm, median NEDT = 26.5 mK] and (b) 98.7% for the 2012 series LWIR [81 K, *f*/3.0 background, integration time (T_{int}) 850 μs, *cutoff* = 5.1 μm, median NEDT = 38.7 mK]. A remarkable improvement in operability for the 2012 series is obtained. This can be seen in the much smaller NEDT frequency tail and much sharper operability curve in the 2012 data.

(81 K, *f*/3.0 background) operability of the 2012 series. Figure 8 shows a comparison between the LWIR operability of 96.1% (85 K, *f*/3.5 background) of the 2009 series and the 98.7% (81 K, *f*/3.0 background) operability of the 2012 series. Experimental conditions (photon fluxes, test temperature, integration time) for FPAs measured in 2009 and 2012 present minor variations, therefore an absolute comparison between them is not achievable. While deviations in the experimental conditions explain the disagreements in the NEDT values presented for these two series, the excellent performance of both series cannot be denied. Comparable MWIR performance for the 2009 and 2012 series is evident. The result for the longer-cutoff 2012 series shows a higher median NEDT value but sharper cumulative curve (Fig. 8b) when compared with the 2009 series (Fig. 8a). As discussed in "Material Growth and Characterization" section, if growth defects were the factor limiting detector performance, less sharp cumulative curves for the 2012 series would be expected. To clarify this point, Fig. 9 artificially plots the operability of FPAs as a function of defect density of the wafer, for different pixel pitches. In this plot, it is supposed that defects are uniformly distributed on the surface of the wafer and that each defect within a pixel degrades the pixel responsivity. As seen from this figure, for FPAs with 60 μm or smaller pitch, more than 99% of the pixels are unaffected by the defect density measured; therefore, if defects are the factor limiting device performance, operability should be near 100% for both bands in both series. Moreover, if growth-related defects are a limiting factor, the 2009 detector

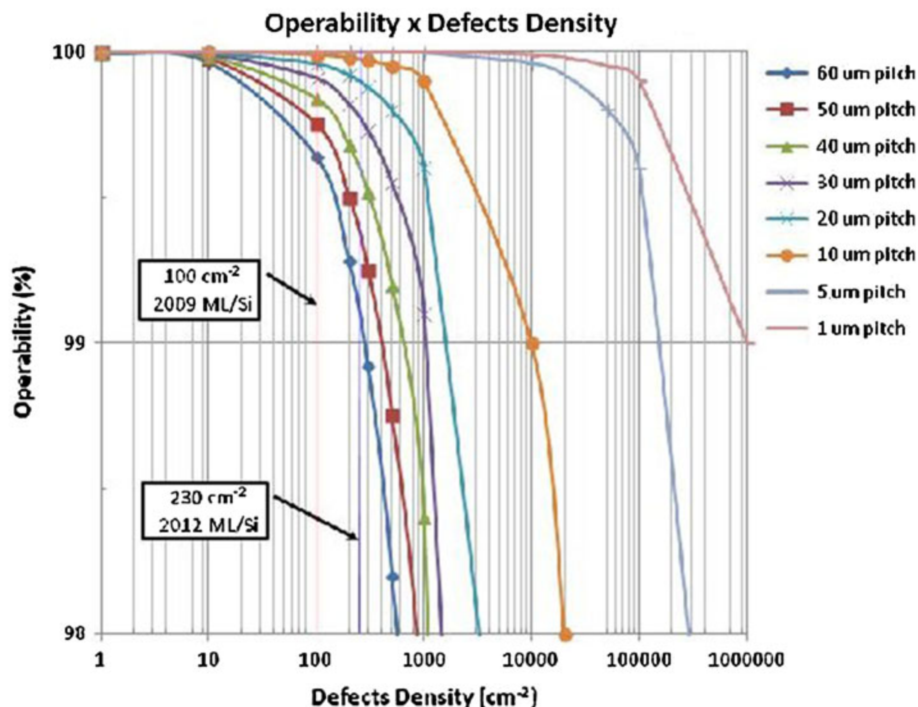

Fig. 9. Operability as a function of defect density with varying pixel pitch. It is proposed that each defect that reaches a pixel of the FPA degrades the response of that pixel. Defect densities obtained in the 2009 and 2012 series are shown in the figure for comparison purposes.

Fig. 10. Video screenshot obtained from band 2 (LWIR) using a camera built with a wafer produced in this work.

series, which has a lower defect density, should have better performance metrics than the 2012 series. Now, using the same reasoning as above for dislocation density, the FPA operability for devices grown on Si wafers, which have dislocation density of $\sim 1 \times 10^6$ cm^{-2}, should be close to 0% for any currently available pixel pitch (>20 μm). The measured operability is 99.98% for the MWIR band and 98.7% for the LWIR band, so the dislocation density should not be the factor limiting FPA operability. The same conclusion was reached by Benson et al.[14] Nevertheless, the dislocation density is believed to be more detrimental for LWIR material response, even though the physics driving this poorer performance is not yet well understood.[15–18,22] Therefore, based on the above-mentioned points, the significantly better performance of band 2 in the 2012 series cannot be explained by any of these measurable properties. It is believed that this improvement in performance is due to process maturity. Additionally, the high performance metric values achieved in both bands were reproduced in more than one wafer in this 2012 series. Figure 10 shows a video screenshot obtained from band 2 using a camera built with a wafer produced in this work.

CONCLUSIONS

M/LWIR dual-band HgCdTe/Si FPA results from Raytheon are presented. A series of M/LWIR dual-band HgCdTe triple-layer *n-P-n* heterojunction device structures were grown by MBE on 100-mm (211)Si substrates. The wafers showed low macro-defect densities (<300 cm^{-2}). Typical 81-K cutoff wavelengths of 5.1 μm for MWIR and 9.6 μm for LWIR were obtained. The FPAs exhibited high pixel operabilities in each band with NETD operabilities up to 99.98% for the MWIR band and 98.7% for the LWIR band at 81 K, at *f*/3 background. These results validate the high quality of Raytheon's HgCdTe/Si dual-band material and indicate that heteroepitaxial HgCdTe/Si shows real promise for large-format dual-band FPAs. For the first time, LWIR devices on large-area Si substrates fulfill the very stringent specification requirements of systems for tactical applications. Data were presented showing that MBE epitaxial growth defects and

dislocation density are not primary limiting factors for device operability in either band for tactical applications. High-operability FPAs can be realized despite higher dislocation density for HgCdTe/Si relative to HgCdTe/CdZnTe. However, HgCdTe/Si is not yet suitable for use in strategic applications. Higher dislocation density impacts LWIR operability more strongly than MWIR operability. Since no measurable entity was evident, the higher FPA operability performance for the 2012 FPAs can be attributed to process maturity. Work will continue towards understanding what limits the operability of the LWIR band with the goal of a higher-yield, lower-cost dual-band technology in the future.

ACKNOWLEDGEMENTS

This work was funded partially by RVS internal research and development (IR&D) and by the US Army RDECOM CERDEC Night Vision and Electronic Sensors Directorate (NVESD).

REFERENCES

1. S.M. Johnson, M.H. Kalisher, W.L. Ahlgren, J.B. James, and C.A. Cockrum, *Appl. Phys. Lett.* 56, 946 (1990).
2. K.D. Maranowski, J.M. Peterson, S.M. Johnson, J.B. Varesi, A.C. Childs, R.E. Bornfreund, A.A. Buell, W.A. Radford, T.J. de Lyon, and J.E. Jensen, *J. Electron. Mater.* 30, 619 (2001).
3. J.B. Varesi, R.E. Bornfreund, A.C. Childs, W.A. Radford, K.D. Maranowski, J.M. Peterson, S.M. Johnson, L.M. Giegerich, T.J. de Lyon, and J.E. Jensen, *J. Electron. Mater.* 30, 566 (2001).
4. J.B. Varesi, A.A. Buell, J.M. Peterson, R.E. Bornfreund, M.F. Vilela, W.A. Radford, and S.M. Johnson, *J. Electron. Mater.* 32, 661 (2003).
5. S.M. Johnson, A.A. Buell, M.F. Vilela, J.M. Peterson, J.B. Varesi, M.D. Newton, G.M. Venzor, R.E. Bornfreund, W.A. Radford, E.P.G. Smith, J.P. Rosbeck, T.J. de Lyon, J.E. Jensen, and V. Nathan, *J. Electron. Mater.* 33, 526 (2004).
6. M.F. Vilela, A.A. Buell, M.D. Newton, G.M. Venzor, A.C. Childs, J.M. Peterson, J.J. Franklin, R.E. Bornfreund, W.A. Radford, and S.M. Johnson, *J. Electron. Mater.* 34, 898 (2005).
7. E.A. Patten, P.M. Goetz, M.F. Vilela, K. Olsson, D.D. Lofgreen, J.G. Vodicka, and S.M. Johnson, *J. Electron. Mater.* 39, 2215 (2010).
8. C.L. Jones, L.G. Hipwood, J. Price, C.J. Shaw, P. Abbott, C.D. Maxey, H.W. Lau, R.A. Catchpole, M. Ordish, P. Knowles, and N.T. Gordon, *Proc. SPIE* 6542, 654210 (2007).
9. P. Abbott, P.M. Thorne, and C.P. Arthurs, *Proc. SPIE* 8012, 801236 (2011).
10. W.A. Radford, E.A. Patten, D.F. King, G.K. Pierce, J. Vodicka, P. Goetz, G. Venzor, E.P.G. Smith, R. Graham, S.M. Johnson, J. Roth, B. Nosho, and J. Jensen, *Proc. SPIE* 5783, 331 (2005).
11. M.F. Vilela, S.F. Harris, R.E. Kvaas, A.A. Buell, M.D. Newton, K.R. Olsson, D.D. Lofgreen, and S.M. Johnson, *J. Electron. Mater.* 38, 1755 (2009).
12. D.D. Lofgreen, J.M. Peterson, A.A. Buell, M.F. Vilela, and S.M. Johnson, *J. Electron. Mater.* 35, 1487 (2006).
13. D.D. Lofgreen, M.F. Vilela, E.P. Smith, M.D. Newton, D. Beard, and S.M. Johnson, *J. Electron. Mater.* 36, 958 (2007).
14. J.D. Benson, L.O. Bubulac, P.J. Smith, R.N. Jacobs, J.K. Markunas, M. Jaime-Vasquez, L.A. Almeida, A.J. Stoltz, P.S. Wijewarnasuriya, G. Brill, U. Lee, M.F. Vilela, J.M. Peterson, S.M. Johnson, D.D. Lofgreen, D.R. Rhiger, E.A. Patten, and P.M. Goetz, *J. Electron. Mater.* 39, 1080 (2010).
15. M. Carmody, J.G. Pasko, D. Edwall, R. Bailey, J. Arias, M. Groenert, L.A. Almeida, J.H. Dinan, Y. Chen, G. Bill, and N.K. Dhar, *J. Electron. Mater.* 35, 1417 (2006).
16. S.M. Johnson, D.R. Righer, J.P. Rosenbeck, J.M. Peterson, S.M. Taylor, and M.E. Boyd, *J. Vac. Sci. Technol.* B10, 1499 (1992).
17. K. Jowikowski and A. Rogalski, *J. Electron. Mater.* 29, 736 (2000).
18. R.S. List, *J. Electron. Mater.* 22, 1017 (1993).
19. S. Farrell, M.V. Rao, G. Brill, Y. Chen, P.S. Wijewarnasuriya, N. Dhar, D. Benson, and K. Harris, *J. Electron. Mater.* 40, 1727 (2011).
20. J.D. Benson, S. Farrell, G. Brill, Y. Chen, P.S. Wijewarnasuriya, L.O. Bubulac, P.J. Smith, R.N. Jacobs, J.K. Markunas, M. Jaime-Vasquez, L.A. Almeida, A.J. Stoltz, U. Lee, M.F. Vilela, J.M. Peterson, S.M. Johnson, D.D. Lofgreen, D.R. Rhiger, E.A. Patten, and P.M. Goetz, *J. Electron. Mater.* 40, 1847 (2011).
21. A.J. Stoltz, J.D. Benson, M. Carmody, S. Farrell, P.S. Wijewarnasuriya, G. Brill, R.N. Jacobs, and Y. Chen, *J. Electron. Mater.* 40, 1785 (2011).
22. P.S. Wijewarnasuriya, Y. Chen, G. Brill, N. Dhar, D. Benson, L.O. Bubulac, and D. Edwall, *J. Electron. Mater.* 39, 1110 (2010).